FEATURE ARTICLE

Charge Transport at Metal−Molecule Interfaces: A Spectroscopic View

X.-Y. Zhu*

Department of Chemistry, University of Minnesota, Minneapolis, Minnesota 55455

Received: October 12, 2003; In Final Form: March 10, 2004

How an electron crosses a metal−molecule interface has been a longstanding question in many disciplines. The prevalence of this question is illustrated by the different terms used to describe essentially the same process: interfacial electron transfer, charge injection, charge transport, and electron attachment to name a few. The recent surge of interest in molecule-based electronics has renewed the need for quantitative answers to this question. In molecule-based conventional electronic devices, such as organic light-emitting diodes, the metal−molecule interface determines the charge-injection efficiency. The importance of the interface only increases as device dimensions shrink to the scale of a single molecule or a small group of molecules (i.e., molecular electronics). This account takes an experimentalist's view and discusses recent progress in understanding electron transport at metal−molecule interfaces using two-photon photoemission (2PPE) spectroscopy. A 2PPE experiment probes interfacial electron transport in energy, momentum, and time spaces. The latter is especially important because the transport of an electron across a metal−molecule interface is an inherently dynamic process occurring on femtosecond time scales. Recent 2PPE experiments allow us to quantify the following concepts critical to the understanding of interfacial effects in molecule-based electronics: (1) the alignment of molecular orbitals to the metal Fermi level; (2) charge redistribution and interfacial dipoles; (3) the strength of electronic coupling; and (4) electronic−nuclear coupling and dynamic localization.

1. Introduction

The problem of interfacial charge transfer is both old and new. This statement becomes clear when one considers the same process in seemingly different research fields: (A) electron transport in nanoscale metal−molecule−metal junctions;[1−3] (B) charge injection at metal−molecule interfaces in organic light-emitting diodes;[4,5] (C) interfacial electron transfer in electrochemistry;[6] (D) hot-electron-mediated photochemical reactions on metal surfaces;[7,8] and (E) electron injection in dye-sensitized solar cells.[9,10] It is not my intention here to provide a detailed discussion of each topic. Interested readers are referred to excellent reviews available on these subjects.[1−10] Instead, I would like to focus on commonalities underlying all of these processes. Such a comparative discussion allows us effectively to define the key issues that need to be tackled by future experiments and theories.

1.1. Electron Transport across Nanoscale Metal−Molecule−Metal Junctions. The "hot" field of molecular electronics is at an early stage of phenomenological demonstration. Quantitative understanding is critically needed for further development. Many of the proposed schemes for molecular electronic devices require making electronic contacts to one or a small group of molecules. Thus, an essential part of this quantitative understanding is the role of metal−molecule contacts is governing charge transport across a molecular junction. Figure 1A shows a typical nanoscale metal−molecule−metal structure in which a single molecule is connected at both ends by metal electrodes (including scanning probe microscope tips). The principal electron-transport mechanisms are believed to be tunneling: molecular orbital (MO)-assisted nonresonant or resonant tunneling via the lowest unoccupied molecular orbital (LUMO) or the highest occupied molecular orbital (HOMO). Scattering theory predicts that the electrical conductance (Ω^{-1}) across such a junction is given by[2,3]

$$g = g_o \, \Gamma_1^{(L)} \, \Gamma_N^{(R)} |G_{1N}|^2 \qquad (1)$$

where $g_o = 2e^2/h = (12.9 \text{ k}\Omega)^{-1}$, the quantum of conductance; $\Gamma_1^{(L)}$ and $\Gamma_N^{(R)}$ (both in units of energy, eV) represent the electronic coupling strength (also called spectral density) between the molecule and the left and right electrodes, respectively, and G_{1N} (eV^{-1}) is the Green's function matrix element for the molecular bridge. Here one assumes that the molecular bridge consists of N weakly coupled units, with unit 1 coupled to the left electrode (L) and unit N coupled to the right electrode (R). This equation clearly shows that the transmission properties of the contacts are as important as the molecular structure in governing electron transport. In fact, the molecular bridge itself can be inseparable from the contacts. Thus, transport across such a nanoscale junction is essentially an interfacial problem. Most theories treat this problem within a coherent electron-transport picture, and electronic coupling strengths at the interfaces are dealt with within chemisorption models. Coupling of the electronic manifold to nuclear motions and to the thermal bath is not included in this equation. One

Feature Article

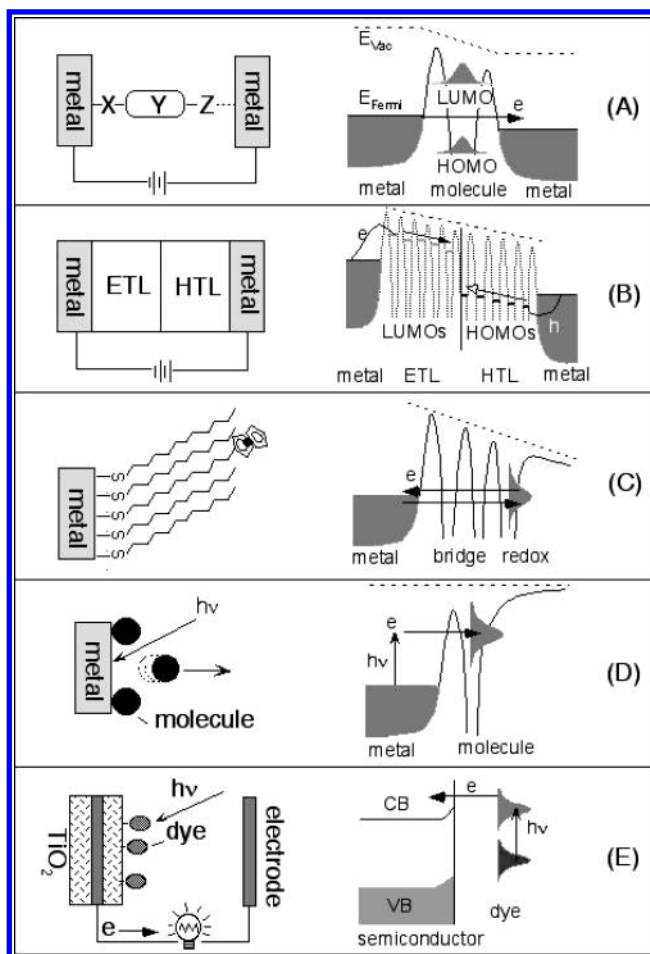*J. Phys. Chem. B, Vol. 108, No. 26, 2004* **8779**

Figure 1. Schematic illustration of various processes involving interfacial electron transport/transfer: (A) tunneling through a metal−molecule−metal nanojunction; (B) charge injection and transport in organic light-emitting devices (OLED) (ETL = electron transport layer, HTL = hole transport layer); (C) electrochemistry of surface-tethered redox species; (D) hot-electron-mediated surface photochemistry; (E) electron injection into a dye-sensitized TiO₂ solar cell.

may argue that this simplification is justified on the basis of the assumption that electron tunneling across such a nanoscale interface occurs on an ultrashort time scale, shorter than what is needed for significant nuclear movement.

1.2. Charge Injection at Metal−Molecule Interfaces in Organic Light-Emitting Diodes. For molecule-based devices on a larger scale, such as an organic light-emitting device (OLED) in Figure 1B, interfacial electron transport also plays a critical role. Here, one often refers to the interface problem as electron (hole) injection at the cathode (anode).[4,5] The efficiency of an OLED can be determined to a great extent by the charge-injection efficiencies. Thus, a number of studies have been devoted to probing and tuning interfacial electronic structure at metal−molecule contacts. Most of these efforts have concerned the energetic alignment of HOMO or LUMO levels with respect to the metal Fermi level, including the possible presence of interfacial dipoles. This alignment determines the so-called energy barrier for electron (hole) injection. Once the electron (hole) has been injected into the molecular layer, further transport occurs via incoherent hopping of a localized charge (i.e., a polaron). Similar hopping transport involving the actual occupation of localized MOs is also possible for metal−molecule−metal junctions in Figure 1A when the molecular bridge is sufficiently long and the electron energy is close enough to a resonance. The OLED literature often calls the

distribution of HOMO or LUMO levels where hopping occurs a HOMO or LUMO "band". Rigorously speaking, the term band used here is different from the concept of electronic bands for crystalline systems in solid-state physics. A more accurate description of the so-called band in typical organic layers in OLED is a distribution of weakly coupled, discrete energy levels due to statistical fluctuation or heterogeneity in the local chemical environment. Note that, whereas past studies on the interface problem in OLED have focused on energetics,[4,5] electron (hole) injection efficiency should also depend critically on the interfacial electronic coupling strength and the coupling of electronic degrees of freedom to nuclear coordinates and the thermal bath. Here, interfacial electronic coupling has the same meaning as the Γ terms in eq 1 for molecular electronics, and coupling to nuclear coordinates and the thermal bath is well established by the polaron theory or the Marcus theory[11] in other contexts. These two issues must also be addressed before a quantitative understanding of electron (hole) injection in OLED is realized.

1.3. Interfacial Electron Transfer in Electrochemistry. The key issues discussed above for molecule-based electronics have been thoroughly discussed in the more mature field of electrochemistry.[6] Figure 1C shows a well-known model system in which a redox species, ferrocene, is tethered with a spacer at a controlled distance to a metal electrode via a self-assembled monolayer (SAM). The presence of the spacer usually leads to weak electronic coupling between the redox species and the metal electrode. Under this condition, the rate constant (s⁻¹) for nonadiabatic interfacial electron transfer is given by[6,11]

$$k_{ET} = \frac{2\pi}{\hbar} \int d\epsilon \, f(\epsilon) \, \rho(\epsilon) |H_{DA}(\epsilon)|^2 \left(\frac{1}{4\pi\lambda k_B T}\right)^{1/2} \times$$
$$\exp\left[-\frac{(\lambda - \epsilon + \eta e)^2}{4\lambda k_B T}\right] \quad (2)$$

where k_B is the Boltzmann constant and T is the temperature. λ is the reorganization energy in the nuclear coordinates; ηe is the applied potential relative to the formal potential of the redox couple; $f(\epsilon)$ is the Fermi−Dirac distribution; ρ is the density of states (DOS) of the metal; and H_{DA} is the electronic coupling matrix element between the metal surface and the redox species. $\rho(\epsilon)|H_{DA}(\epsilon)|^2 = |V(\epsilon)|^2$ is the metal DOS-weighted and k-space-integrated electronic coupling strength, which can be approximated by its value at the Fermi energy (E_F) (i.e., $|V(E_F)|^2$). This is justified because one is interested only in states near the Fermi level in a typical electrochemical process. Within this Marcus picture,[11] the interfacial electron-transfer rate is directly proportional to $|V(E_F)|^2$. However, unlike eq 1, eq 2 contains the thermal activation term; it originates from the Boltzmann-weighted Franck−Condon factor. Thermal fluctuation in nuclear coordinates is responsible for bringing the redox species into resonance with the metal Fermi level for electron transfer. Such a dominating nuclear factor is missing in the coherent tunneling picture in eq 1 because in the latter case the tunneling electron does not reside in a localized molecular orbital. Note that, in contrast to the well-established picture of interfacial electron transfer in the weak-electronic-coupling limit, strong electronic coupling is much less understood. This arises because of the limited time resolution of a typical electrochemical experiment and because of the absence of a well-tested adiabatic electron-transfer theory for interfacial processes.

1.4. Hot-Electron-Mediated Surface Photochemistry. Interfacial electron transfer and electronic−nuclear coupling are central issues in photochemistry on metal or semiconductor

surfaces.[7,8] Figure 1D illustrates such a mechanism for photo-desorption from a metal surface. Photon absorption by the metal substrate creates a transient distribution of hot electrons. A hot electron can be transferred to a molecular resonance (e.g., LUMO); this is often called "hot-electron attachment". Although both back electron transfer from the molecular resonance to the metal and the relaxation of hot electrons to the Fermi level occur on femtosecond time scales, sufficient nuclear movement can occur within the ultrashort lifetime of the transient anion. This transfer of energy from electronic excitation to nuclear coordinates can result in chemical changes (desorption or dissociation), albeit with low yield. An important lesson learned from surface photochemistry is that interfacial electron transfer and electronic−nuclear coupling can both occur on an ultrafast time scale. Such a fast dynamic process leads to the breakdown of the Born−Oppenheimer approximation, although this approximation was often used in the "sudden transition and averaging" model of hot-electron-mediated surface photochemistry.[8] Refinements to the sudden transition approach can be found in the surface hopping model of Tully[12] or the electronic friction model for desorption induced by multiple electronic transitions.[13]

1.5. Electron Injection in Dye-Sensitized Solar Cells. In dye-sensitized nanocrystalline semiconductor solar cells (i.e., Gratzel cells (Figure 1E)), photovoltaic conversion is achieved via electron injection into the conduction band of semiconductors from photoexcited dye molecules anchored to semiconductor surfaces.[9] A very similar process occurs in the much older field of photographic chemistry, which is based on charge transfer between photoexcited dye molecules and silver halides The most successful type of Gratzel cells uses nanocrystalline TiO_2 and tris(2,2′-bipyridyl, 4,4′-carboxylate) Ru(II) dye.[9] The carboxylate groups provide covalent anchors and are critical in ensuring significant electronic coupling and ultrafast electron injection, which occurs on a sub-100-fs time scale.[10] The key factors discussed above for metal−molecule interfaces are of equal importance here. They include electronic coupling strength, energetic alignment (also called energetic driving force), dynamics in nuclear coordinates (e.g., vibrational relaxation), and density of semiconductor states.[10] Despite extensive studies, the critical factor—interfacial electronic coupling—remains poorly understood in these systems. This arises in part from difficulties in characterizing and controlling structure and bonding at molecule/solid interfaces in the majority of experiments using nanostructured semiconductors in solution phases.

This account reviews recent progress in understanding the key issues in electron transport at metal−molecule interfaces using two-photon photoemission spectroscopy. Several salient features of this experimental approach are noteworthy: (i) the model systems involve well-characterized probe molecules adsorbed on single-crystal metal surfaces in an ultrahigh vacuum environment; (ii) the technique directly probes the electron in energy and momentum spaces; (iii) the femtosecond time resolution is compatible with ultrafast dynamics in both electronic and nuclear coordinates during interfacial electron transport; and (iv) the technique is inherently sensitive to strong electronic coupling. The article is organized as follows. A brief overview of existing theories related to interfacial electron transport and transfer is presented first. This is followed by a discussion of the experimental technique of 2PPE. Next, key issues in interfacial electron transport that have been probed by 2PPE are discussed in detail. Finally, some comments on the role of surface spectroscopies in advancing the field of molecular electronics are presented.

Note that the terms electron transfer and electron transport are favored by different communities. In chemistry and biology, electron transfer usually refers to the movement of an electron from a localized initial state to a localized final state, where the localization comes from nuclear coordinates. Electron transport is usually used in the physics community to describe the movement of electrons in metal or semiconductor structures where nuclear localization is of much less significance. However, these are only two limiting cases, and it is not very meaningful to provide a rigorous distinction. Note also that I focus on electrons in normally unoccupied states. Hole transport is equivalent to electron transport via occupied states and is more difficult to probe from a spectroscopic perspective. It will remain a challenge for future experiments.

2. Theories

The theoretical treatment of interfacial electron transport can be divided into two categories: standard electron-transfer theory such as eq 2, which gives the rate constant, k_{ET} (s^{-1}), and transport theory exemplified by eq 1, which gives the conductance, g (Ω^{-1}). Nitzan and Ratner recently presented a concise review of state-of-the-art electron-transport theories for molecular junctions.[3] In a more detailed (and excellent) account, Nitzan also illustrated the intimate relationship and fundamental differences between electron-transfer and electron-transport theories.[2] In addition to electron-transport and electron-transfer theories, I will briefly review other relevant theories, including polaron theory for charge-carrier localization in molecular solids and image potential state theory on metal surfaces.

2.1. Standard Electron-Transfer Theory. For electron transfer between a molecular donor (D) state and a molecular acceptor (A) state in the weak-electronic-coupling limit, the common starting point for the electron-transfer rate is the golden-rule approach:[2,6,11]

$$k_{ET} = \frac{2\pi}{\hbar} |H_{DA}|^2 (FC) \tag{3}$$

where H_{DA} is the electronic coupling matrix element between the donor and the acceptor and FC is the thermally averaged Franck−Condon factor between a Boltzmann distribution of donor nuclear states and all acceptor nuclear states. It can be easily shown that, at the high-temperature limit, FC reduces to[6,11]

$$FC = \left(\frac{1}{4\pi\lambda k_B T}\right)^{1/2} \exp\left[-\frac{(\lambda + \Delta G^\circ)^2}{4\lambda k_B T}\right] \tag{4}$$

where ΔG° is the free-energy difference between the acceptor and the donor and λ, the reorganization energy, is the energy difference between the acceptor and the donor if the system makes an instantaneous, vertical (i.e., with nuclear coordinates frozen) jump from the donor state to the acceptor state. When a discrete molecular donor (acceptor) is replaced by a metal electrode, one needs to integrate over all of the occupied (unoccupied) metal states. Equation 3 then becomes eq 2, where ΔG° is replaced by electron energy below (above) the Fermi level plus the bias potential; the electronic-coupling matrix element is weighted by the metal DOS. Tunneling through the spacer is reflected in the distance (d)-dependent relationship of electronic coupling:

$$|H_{DA}|^2 \propto \exp(-\beta d) \tag{5}$$

where the β values (measured mostly from electrochemistry

Feature Article

J. Phys. Chem. B, Vol. 108, No. 26, 2004 **8781**

experiments) have been found to lie in the range of $0.9-1.3$ $Å^{-1}$ for saturated alkanes and to be as small as 0.2 $Å^{-1}$ for some π-conjugated molecules.[14] Recent experiments by Frisbie and co-workers showed similar β values for metal−molecule−metal junctions.[15] This exponential dependence of the electron-transfer rate on the donor−acceptor distance is expected for tunneling. One may also derive eq 5 from first principles (e.g., the super-exchange model that assumes that electronic states on the spacer (also called bridge) are much higher than the energy of the transmitted electron and are not coupled to the thermal bath).[2]

For strong electronic coupling between a donor state and an acceptor state, electron transfer occurs adiabatically (i.e., on the same potential energy surface). The electronic coordinate equilibrates with the nuclear coordinate. Electron transfer is essentially described by a time-dependent charge redistribution of the mixed state, localized to the donor or the acceptor potential well due to nuclear fluctuation. There is an effective energy barrier, E^*, between the donor well and the acceptor well. The electron-transfer rate constant is given by[6]

$$k_{ET} = AC \exp\left(-\frac{E^*}{k_B T}\right) \tag{6}$$

where the preexponential factor A (s^{-1}) is the frequency of a fast nuclear mode responsible for ET, often assigned as the longitudinal relaxation frequency of the solvent; C is a constant that converts bulk concentration to surface concentration. Because the discrete molecular donor (acceptor) is replaced by a metal electrode, one in principle needs to integrate over all of the occupied (unoccupied) metal states. However, within the finite width of the molecular resonance, E^* can be treated as energy-independent.

Adiabatic ET is often discussed in three regions depending on the magnitude of electronic coupling, Δ.[6] When $\Delta \ll 2\lambda/\pi$, Δ has little effect on E^*, which is essentially determined by the reorganization energy λ. When $k_B T < \Delta \leq 2\lambda/\pi$, E^* is significantly lowered by electronic coupling, and the ET rate is a strong function of Δ. Finally, when $\Delta > 2\lambda/\pi$, E^* becomes negligible, and the donor and the acceptor can no longer be distinguished. These distinctions demonstrate the critical importance of Δ in determining interfacial electron transfer with strong electronic coupling. Quantum chemical treatments of adiabatic potential energy surfaces for ET and the electronic coupling terms have been carried out within the framework of chemisorption theories, such as the Newns−Anderson model.[16,17]

Note that in most electron-transfer processes or the equivalent process of small-polaron hopping in molecular solids[18,19] the electronic coupling or transfer energy (Δ) is small, typical <1 meV, because the transfer of an electron or the hopping of a small polaron requires the movement of not only the charge but also the associated nuclear displacement. In comparison, the interfacial spectral density terms (Γ) in the electron-transport equations can be >1 eV because they are measures of direct interaction/mixing of electronic wave functions, without the need for nuclear movement. This is the strong-coupling limit $(\Delta > 2\lambda/\pi)$ discussed above and corresponds to femtosecond or subfemtosecond lifetimes. Strictly speaking, there is no electron transfer between the metal and the strongly coupled adsorbate orbital. If one must speak of electron transfer in this strong-coupling limit, it is essentially a dephasing process between an adsorbate resonance and continuum states in the metal electrode. Such ultrashort lifetimes or ultrafast electron "transfer" rates have been successfully probed by the so-called "core hole clock" method in core-level photoemission spectroscopies.[20−22]

2.2. Conduction at Metal−Molecule−Metal Junctions. To derive the tunneling current−voltage characteristic of a metal−molecule−metal junction, one may start with a number of approaches, including the well-known WKB approximation, the Bardeen formalism, and the more general Landauer equation.[2] Landauer considered conduction through a 1D conductor contacted by two macroscopic electrodes.[23] At the zero Kelvin temperature and zero volt bias limit, the conductance g is given by[2,3,23]

$$g = \frac{2e^2}{h} T(E_F) \tag{7}$$

where T is the transmission function. If directions normal to the lead are included, then one needs to sum over all scattering channels corresponding to transversal modes on the left electrode to those on the right electrode. When the 1D lead is a molecular bridge, the transmission function can be expressed as

$$T = \Gamma_1^{(L)} \Gamma_N^{(R)} |G_{1N}|^2 \tag{8}$$

Substituting eq 8 into eq 7 gives eq 1. The two width factors (Γ) correspond to electronic coupling strengths on the two electrodes and are obtained from electronic structural calculations for chemisorption. For example, in the Newns−Anderson chemisorption theory, the interaction of a discrete atomic or molecular orbital with the electronic band of a metal leads to a broadened adsorbate resonance.[24] In the simplest case when the adsorbate level is located in the middle of a broad sp band, the density of states (DOS) of the adsorbate resonance is a Lorentzian function with width Γ. Another way of looking at Γ is that it is the inverse of the lifetime (τ) of an electron or hole in the adsorbate resonance:

$$\Gamma = \frac{\hbar}{\tau} \tag{9}$$

The Green's function matrix element through the molecule, G_{1N}, is well known from solution-phase electron-transfer theory. For example, when the energy of the tunneling electron is far from the positions of MOs, the super-exchange model predicts an exponential distance dependence for $|G_{1N}|^2$ (i.e., eq 5). For a metal−molecule−metal junction under bias voltage, one needs to integrate over the energy range defined by the bias to obtain the total current.

It is instructive to compare the standard electron-transfer theory in eq 2 or 3 to the molecular conductance equation (eq 1). Equation 2 or 3 includes the electronic coupling term and a Boltzmann-weighted Franck−Condon factor; the latter results from the actual residence of the electron in vibronic manifolds of donor and acceptor electronic states. However, eq 1 contains only the electronic coupling term, which is equivalent to the bridge-tunneling part of the ET rate in eq 5. The Franck−Condon factor is missing because the transported electron does not reside in a molecular orbital. A common interpretation of eq 1 is that the transported electron tunnels coherently from the left electrode to the right electrode. This picture is incomplete because one should also expect incoherent channels due to dephasing and relaxation.[2,3] They may result from electronic−nuclear coupling (both intramolecular and thermal motions of the environment). Note that the electronic−nuclear coupling discussed here is different from the terms containing nuclear reorganization energy in eq 2. In standard electron-transfer theory, nuclear manifolds come into play only in the form of initial and final states. In the tunneling picture for molecular

electronics, one is interested in dynamic coupling (i.e., during the short time the tunneling electron is within the molecular bridge). Evidence for inelastic tunneling is abundant in other contexts[25] (e.g., the observations of vibrational excitation in inelastic tunneling spectroscopy,[26] including its manifestation at the single-molecule level,[27,28] and surface photochemistry due to hot-electron scattering off of a molecular resonance[7,8]).

Recent theoretical analysis by Segal et al. has extended the Landauer equation to incoherent processes.[29,30] One may start with the formal relationship between conductance and electron-transfer rate:

$$g = e^2 \, k_{ET}(E_F) \, \rho(E_F) \tag{10}$$

where ρ is the density of initial electronic states in the metal electrode; k_{ET}, the steady-state ET rate, can have both coherent tunneling and incoherent hopping contributions

$$k_{ET} = k_{tun} + k_{hop} \tag{11}$$

However, these are two limiting cases. One may view all other incoherent mechanisms as intermediate channels between these two limits.

The importance of incoherent channels can be judged from the time scale it takes for an electron to cross the molecular bridge, the so-called "tunneling traversal time". Nitzan estimated that for a typical molecular junction $\sim$10 Å in length and with an MO $\sim$1 eV above the energy of the tunneling electron the tunneling traversal time is $\sim$0.2 fs.[2] It is significantly shorter than typical time scales for a molecular vibration period. Under this condition, it is a good approximation to ignore incoherent channels. However, when the energy of the tunneling electron is at or near that of a molecular orbital (resonance), the tunneling traversal time can be lengthened substantially. Inelastic scattering/dephasing may become a significant if not dominant event. In another context, such resonance assistance is often invoked in the interpretation of vibrational excitation or surface photochemistry due to inelastic electron scattering.[25] Although a rigorous treatment of inelastic tunneling implies the breakdown of the Born–Oppenheimer picture, approximate methods are feasible (e.g., a perturbation approach[2] of adding a nuclear coupling contribution to the electronic coupling term in eq 1 or a semiclassical wave packet approach[25,31] based on the finite lifetime of the electron in the negative ion molecular resonance). Seideman recently provided an excellent overview of current-triggered dynamics in different contexts.[32]

2.3. Polarons. Perhaps the most important difference between an electron in a molecular phase and an electron in a metal or inorganic semiconductor is the strong tendency of localization in the former. To understand how an electron crosses the metal/molecular interface, one must deal with localization in the molecular phase. In the following, I summarize qualitative aspects of polaron theory in molecular solids. Details can be found in the excellent book of Silinsh and Capek on the electronic properties of organic solids[33] or in the original work of Holstein[18] and Emin[19] on small polarons.

For an excited electron in a molecular solid, there are two competing trends: delocalization and localization. Delocalization is determined by resonant electronic interaction between neighboring molecular orbitals. It is characterized by the electron-transfer integral between neighboring molecules, J_M, which determines the electronic bandwidth $\Delta\epsilon_B$ ($\Delta\epsilon_B \approx 4J_M$ in the Huckel approximation). J_M is on the order of a few tenths of an electronvolt in typical molecular solids, such as polyacenes. The uncertainty principle dictates that the localization of the

electron wave function from such a delocalized state requires paying an energetic penalty of δE_{del}, which is approximately half of $\Delta\epsilon_B$.

The opposite trend is localization due to polarization in electronic and nuclear coordinates. It is a dynamic process occurring on the time scale of the motions involved. An excess electron induces the redistribution of electron density on neighboring molecules. Such an electronic polarization process occurs on the time scale of the inverse of the Bohr frequency (i.e., $\tau_e \approx 10^{-16}$–10^{-15} s), which can also be obtained from the uncertainty principle using the electronic excitation energy of $\sim$2–3 eV. For comparison, the time scale for the electron to hop from one molecular site to the other is given by $\tau_h \approx \hbar/J_M \approx 10^{-14}$ s, which is substantially longer than τ_e. Thus, one can view electronic polarization as electrostatic attraction between a fixed electron and induced dipoles in surrounding neutral molecules. Such an electrostatic attraction potential creates a localized trap for the electron (i.e., an electronic polaron) with energetic gain on the order of 1–1.5 eV in typical molecular solids, such as polyacenes. The polarization of nuclear subsystems occurs on a longer time scale. There are two main flavors: intramolecular and lattice polaron formation. The polarization of intramolecular coordinates results in a molecular polaron. If dipole-active vibrational modes in neighboring molecules are also involved in trapping the molecular polaron, then the net result is a nearly small molecular polaron. The typical interaction energy of a molecular polaron is 0.1–0.2 eV, and the time scale is on the order of $\tau_v \approx 2 \times 10^{-15}$–$2 \times 10^{-14}$ s (molecular vibrations). If lattice vibrations (optical and acoustic phonons) are involved, then the result is a lattice polaron, with an interaction energy of $<$0.1 eV and a time scale of $\tau_l > 10^{-13}$ s.

These polarization effects lead to an energy gain for localization, δE_{pol}, which is dominated by the electronic part. An additional localization effect comes from the direct bonding of the electron to the molecule, forming a molecular anion, with an energy gain of δE_b. Under most conditions, the following inequality is satisfied

$$|\delta E_{del}| < |\delta E_{pol} + \delta E_B| \tag{12}$$

and the electron is localized in the molecular phase. Another way of looking at localization is that the mean free path ($\bar{l}$) of the electron in the molecular solid is usually not longer than the lattice parameter (a_o):

$$\bar{l} \leq a_o \tag{13}$$

The above picture is modified when the molecules are in close proximity to a metal surface. For molecules in direct contact with or chemically bonded to the metal, there is an additional contribution of delocalization due to the mixing of molecular wave functions with electronic bands in the metal. This leads to the substrate-mediated delocalization of an electron in the molecular layer. In other words, the molecules "borrow" delocalization from the metal substrate. The presence of the metal surface also contributes to localization because electron density in the metal is easily polarized by the excess electron in the molecular layer. This is essentially the image potential discussed in the next section. Such an image potential serves to localize the electron in the direction perpendicular to the surface but not in the surface plane.

Theoretical treatments of charge localization and polaron formation may be divided into two classes dealing with electronic and nuclear polarizations, respectively. Because the
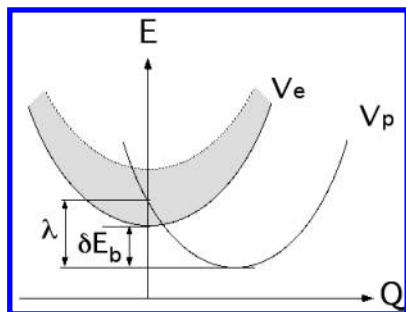
Feature Article

J. Phys. Chem. B, Vol. 108, No. 26, 2004 **8783**

Figure 2. Schematic potential energy surfaces for polaron formation in a molecular solid. Q is a generic nuclear coordinate; V_e and V_p are potential energy surfaces before and after nuclear localization; the shaded region on V_e represents the bandwidth (in k space) of the electronic polaron; and λ is the polaron relaxation energy.[33]

Figure 3. Schematic presentation of the image potential and the resulting Rydberg states ($n = 1, 2, 3,...$) on a single-crystal metal surface. A project band gap is also shown. The inset illustrates the polarization of charge density in the metal by an excess electron above the surface.

electron hopping time is much longer than the electronic polarization time, $\tau_h \gg \tau_e$, a simple theory for treating electronic polarization is the microelectrostatic approximation (also called the Mott–Littleton theory), which views the excess charge as a static point charge. The electronic polarization energy is calculated by classical electrostatics for the point charge and induced dipoles in surrounding neutral molecules. More accurate treatments come from dynamic approximations that assume that the movement of the excess charge is not too fast so that it interacts fully (i.e., equilibrates) with the electronic subsystems of the surrounding. Such an interaction may be represented by a frequency-dependent dielectric constant. This kind of dynamic theory leads to delocalization and Bloch waves of the electronic polaron, which is a quasi-particle consisting of the charge carrier dressed by its polarization cloud. Both static and dynamic approximations are valid for $\tau_h \gg \tau_e$. When the charge carrier is highly excited (very hot), τ_h may approach τ_e, and the single-electron picture inherent in these approximations breaks down.

Polarization in nuclear coordinates includes molecular/nearly small molecular polarons and lattice polarons. Because the electron hopping time is usually longer than the time scale for molecular vibration, $\tau_h \geq \tau_v$, the formation of a molecular or nearly small molecular polaron is a competitive process. However, the hopping time is usually shorter than the lattice interaction time, $\tau_h < \tau_l$, for solids of most conjugated molecules. Thus, a lattice polaron does not have sufficient time to form before the localized carrier hops to neighboring sites. Only in solids with sufficiently small J_M can τ_h be large enough to allow lattice polaron formation.

The formation of a molecular, a nearly small molecular, or a lattice polaron can often be described by an activation model shown schematically in Figure 2. Here, Q is a generic nuclear coordinate (e.g., molecular vibration), and V_e and V_p are potential energy surfaces before and after nuclear localization. The shaded region on V_e represents the bandwidth (k space) of the electronic polaron, and λ is the polaron relaxation energy if the system makes an instantaneous transition from V_e to V_p; it is also called nuclear reorganization energy in electron-transfer theory (section 2.1). $\delta E_b(k)$ is approximately the molecular polaron binding energy (neglecting the difference in zero-point vibrational energies on V_e and V_p) and is dependent on the momentum vector k within the electronic polaron band. In this activation model, the rate constant for polaron formation is given by

$$k_p = A \exp\left\{-\frac{[-\delta E_b(k) + \lambda]^2}{4\lambda k_B T}\right\} \qquad (14)$$

where the preexponential factor A is related to electronic coupling and the frequency of the motion involved. This
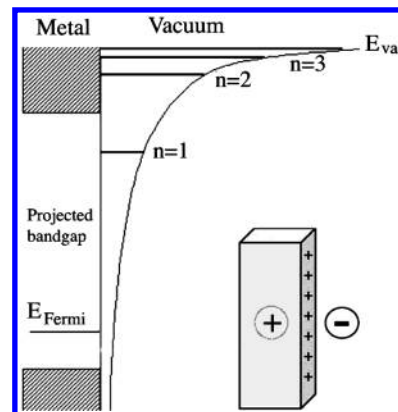
formulation for thermally activated polaron formation is equivalent to the electron-transfer theory in eqs 3 and 4.

2.4. Image Potential States. There is a class of electronic states unique to the metal surface: image potential states.[34,35] Image potential states may play important roles in electron transport at metal–molecule interfaces or serve as models for understanding interfacial electron dynamics. Consider an excess electron above a metal surface (Figure 3). It polarizes charge inside the metal, resulting in an attractive interaction between the electron and the polarized charge density. For a perfect metal with infinite polarizabililty, the net result is equivalent to that of a Coulomb potential between the electron and a fictitious positive image charge (hence the name "image potential states") at $-z$ inside the metal

$$V_{im} = E_{vac} - \frac{e^2}{4\pi\epsilon_o}\frac{1}{4z} \qquad (15)$$

where ϵ_o is the vacuum permittivity. For some metal surfaces, a projected band gap may exist in the surface normal direction; the electron is confined by the image potential on the vacuum side and the energy barrier on the metal side. This is essentially a 1D hydrogen atom problem, the solution of which gives a series of Rydberg states converging to the vacuum level (Figure 3):

$$E_n = E_{vac} - \frac{m_e}{32}\left(\frac{e^2}{4\pi\epsilon_o\hbar}\right)^2\frac{1}{(n+a)^2} \qquad (16)$$

where n is the quantum number; the parameter a, called a "quantum defect", results from the fact that the barrier on the metal side due to the projected band gap is not an infinitely hard wall. There is tunneling of the image electron through the finite barrier, leading to mixing of the hydrogenic wave function with periodic waves in the metal substrate. Such a "leaky" barrier is responsible for femtosecond lifetimes of image potential states.

The image potential confines the electron only in the surface normal direction, not in the surface plane. As a result, image potential states exhibit free-electron-like parallel dispersions:

$$E_n(k_{||}) = E_n + \frac{\hbar^2 k_{||}^2}{2m_{eff}} \qquad (17)$$

where $k_{||}$ is the parallel momentum vector and m_{eff}, the effective electron mass, is close to the free-electron mass, m_e.
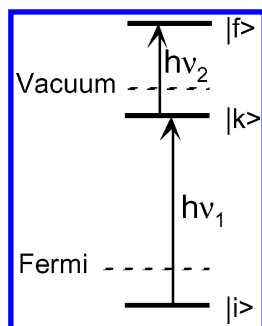
Figure 4. Schematic illustration of the two-photon photoemission process.

Because $|\Psi|^2$ for the image electron is located predominantly within a few angstroms above the metal surface, it serves as an excellent probe of interfacial electronic structure and dynamics.[36-39] Moreover, the image potential is universally present and should be taken into account when we consider the transport of an electron across the metal/molecule interface. For an electron in an adsorbate resonance on a metal surface, the electron experiences not only the atomic/molecular potential but also a superimposed image potential. This concept is successfully demonstrated in the simulation of interfacial and image potential states with atomistic details for rare-gas-covered Cu-(100) surfaces.[40,41]

2.5. Unresolved Issues. The theories summarized above form the foundation of the current understanding of electron transport (transfer) at metal/molecule interfaces. However, they are by no means conclusive and final. Further advancement of our understanding requires not just the development of more accurate theories but, more importantly, the continued testing and challenging of these theories. For example, the electronic coupling strength in the weak-coupling case is well established in theoretical models, and their prediction of an exponential dependence on bridge length has been tested by various experiments. The same cannot be said about strong electronic coupling. The second example, the role of nuclear coordinates in interfacial electron transfer, is described successfully by Marcus theory in terms of the Boltzmann-weighted nuclear density of states of the donor and the acceptor. This beautiful theory has stood the test of numerous experiments. In contrast, little is known about electronic–nuclear coupling during tunneling through a molecular bridge or a metal–molecule–metal junction. As another example, although the image potential is universally present and is particularly important for nanometer-scale metal–molecule–metal junctions, the many-body problem makes it difficult to incorporate into treatments of electron transport theories. These examples illustrate some of the limitations of current theories and experiments on electron transport (transfer) at metal/molecule interfaces. It is the purpose of this account to introduce an experimental approach, namely, time-resolved two-photon photoemission spectroscopy of molecule–metal interfaces,[42-44] that has the potential to fill some of the critical gaps in past experiments and provide quantitative tests and challenges to theories on interfacial electron transport/transfer.

3. Two-Photon Photoemission Technique

3.1. Principle. The principle of the two-photon photoemission technique is illustrated in Figure 4.[36-45] The first photon excites an electron from an occupied state, $|i>$, to a normally unoccupied state, $|k>$. The second photon excites the electron from the transiently populated state, $|k>$, to a final state, $|f>$, above the vacuum level. Here the initial state can be an occupied bulk state of the metal or semiconductor substrate, an occupied surface state, or an occupied molecular state. The intermediate state can be an unoccupied molecular state, an image potential state, or a mixed state resulting from the coupling of molecular orbital to the image potential state or surface states (i.e., chemisorption). The final state is a free-electron state.

The direct photoexcitation mechanism illustrated in Figure 4 requires a nonvanishing transition dipole moment for each step. Although quantitative relationships between the 2PPE signal and the transition dipole moments, the pump–probe delay time, and the relaxation/dephasing rates can be established on the basis of optical Bloch equations, as detailed elsewhere,[46] we restrict our attention to qualitative discussions here. One of the requirements for a nonvanishing transition dipole moment is that there must be spatial overlap in the wave functions involved in each step. For the first photoexcitation step, this requirement can be met with three possible combinations of $|i>$ and $|k>$ (Figure 5). In Figure 5A, the initial state is a pure bulk metal state; thus, the intermediate state $|k>$ must have nonzero probability density inside the metal. This is true if $|k>$ is an image potential state or an unoccupied molecular state with relatively strong coupling to the metal substrate. Because of the presence of a continuum of bulk states, we do not expect to see an excitation resonance with respect to photon energy. In Figure 5B, the initial state is an occupied surface state that originates from bulk states at the metal surface because of broken translational symmetry. A surface state has substantial probability density at the surface. As a result, the intermediate state can be a molecular state or an image potential state with substantial probability density near the surface. Electronic coupling between the molecular state and the metal substrate is not a prerequisite in this case. Because the surface state also has a well-defined energy level, not a continuum, mechanism B requires that the excitation photon energy be resonant with the energy difference between the states involved. In Figure 5C, the first step is a direct intramolecular or intermolecular excitation (e.g., Frenkel or charge-transfer excitons in molecular solids). Electronic coupling between the molecule and the metal substrate is not required and, similar to the situation in B, $h\nu_1$ must be resonant with the discrete molecular energy levels involved.

In addition to the three direct photoexcitation mechanisms in A–C, the intermediate state can also be populated by indirect channels. The first photon excites hot electrons in the metal substrate. The intermediate state, $|k>$, may be populated via the inelastic or quasi-elastic scattering of a hot electron (Figure 5D). Alternatively, the intermediate state may also be populated from the relaxation of a higher-lying state that is excited by the first photon. The indirect mechanism differs from a direct mechanism in terms of coherence. Coherence is lost in scattering events in the indirect mechanism, it is partially preserved within the dephasing time of the intermediate state for the direct mechanism. Experimentally, the indirect mechanism can be distinguished from direct photoexcitation mechanisms based on the dependence of the photoemission signal on light polarization.[46]

3.2. What Is Measured? A 2PPE experiment probes interfacial electronic structure and dynamics in three spaces: energy, momentum, and time. The first type of experiment is simply spectroscopy (i.e., the photoemission intensity is measured as a function of the kinetic energy of the electron). This experiment allows one to determine the energetic position of the normally unoccupied intermediate state from the kinetic energy of the electron. Note that coherent two-photon absorption by an occupied state below the Fermi level can also lead to the
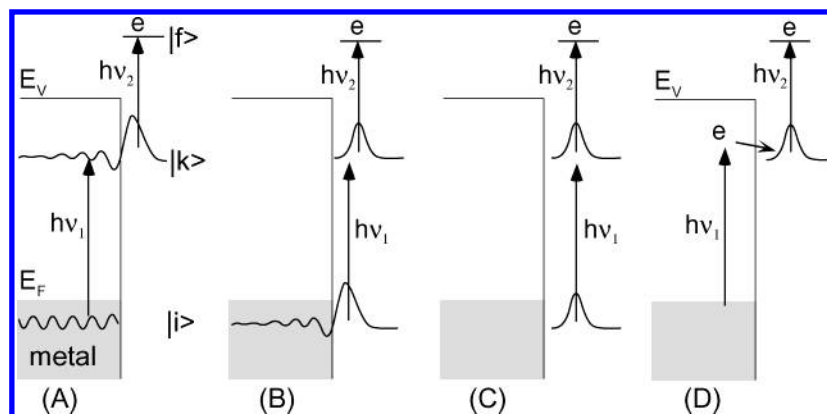
Figure 5. Possible scenarios for the transient population of an intermediate state in two-photon photoemission at molecule−metal interfaces.
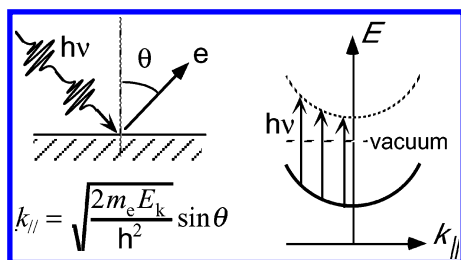

Figure 6. Schematics of angle-resolved 2PPE measurement to give dispersion parallel to the surface. The relationship of the parallel momentum vector ($k_{||}$) to the electron detection angle (θ) and kinetic energy (E_{kin}) is shown.

Figure 7. Time-dependent relaxation in the energy domain of a transiently populated state in 2PPE.

Figure 8. Time-dependent relaxation in the energy and momentum ($k_{||}$) domains of a transiently populated state.

ejection of a photoelectron (via a virtual state). This scenario can be easily distinguished from that involving an unoccupied intermediate state on the basis of the dependence of photoelectron energy on photon energy. In the absence of dispersion in the surface normal direction,[47] which is true for surface or interfacial states, the change in the electron kinetic energy (E_{kin}) scales with that of the second photon (i.e., $\Delta E_{kin} = \Delta h\nu_2$ (or $\Delta h\nu$ in a one-color experiment)) for 2PPE involving a normally unoccupied intermediate state. For 2PPE involving a virtual state, ΔE_{kin} scales with the change in both photon energies (i.e., $\Delta E_{kin} = \Delta h\nu_1 + \Delta h\nu_2$ (or $2\Delta h\nu$ in a one-color experiment)).[36,37,44]

The second type of experiment (Figure 6) probes the dispersion of the state in the surface plane from angle-dependent measurements. This experiment is based on the principle that the parallel momentum of an electron is conserved in the photoemission process. By varying the angle of detection (θ, from the surface normal), one can obtain the parallel momentum vector ($k_{||}$). A plot of E_{kin} versus $k_{||}$ thus gives the parallel dispersion, which is a quantitative measure of the extent of delocalization of the electronic state. One can often fit the experimental data of parallel dispersion to a free-electron-like parabolic relationship (eq 17). The effective electron mass is a quantitative measure of the extent of localization/delocalization.

The third type of experiment probes the dynamics of the electron. Here, the energetics and the dispersion of the transient electronic state are measured as a function of the pump−probe delay time with femtosecond resolution. Several variations are possible. In one approach, photoelectron intensity at a fixed kinetic energy and detection angle is measured as a function of the pump−probe delay time. It probes the lifetime or decay rate of the electronic state at a particular energy and parallel momentum. In the second approach (Figure 7), 2PPE spectra are measured at various pump−probe delay times, and the decrease in peak position (electron kinetic energy) as a function of time provides a measure of the dynamic relaxation of the
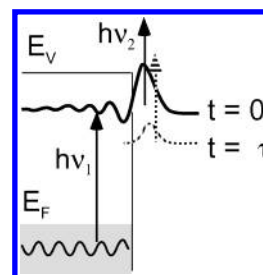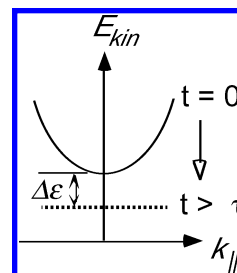
excited electron (e.g., coupling of the electronic coordinate to nuclear motions[48]). The third approach probes parallel dispersion as a function of pump−probe delay. This experiment is valuable in establishing the dynamics of localization (e.g., from a delocalized image or conduction-band electron to a localized polaron). Two important quantities are obtained from this experiment, as illustrated in Figure 8: the rate ($1/\tau$) of relaxation from a delocalized electron (with parallel dispersion) to a localized polaron (without dispersion) and the energetic gain ($\Delta\epsilon$) from such a localization process.[42] In another approach, phase-sensitive detection schemes (e.g., interferometric time-resolved 2PPE) can also be used to establish the dephasing dynamics of the transient electronic state.[45]

Details on the experimental setup can be found elsewhere.[36−48] Briefly, a time-resolved 2PPE experiment is carried out in an ultrahigh vacuum chamber equipped with a hemispherical analyzer or time-of-flight spectrometer for energy- and angle-resolved electron detection. Short laser pulses with a pulse width ≤100 fs are typically generated with a mode-locked Ti:sapphire laser. The visible or near-IR radiation is frequency doubled or tripled to the ultraviolet (UV) region via second- or third-harmonic generation in nonlinear crystals. The UV pulse can be split with equal intensity for pump−probe measurements. Alternatively, a UV pulse and a visible/near-IR pulse (residual output at the fundamental laser frequency) can be used as the pump and the probe, respectively.
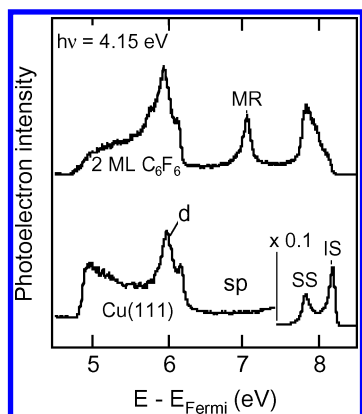
Figure 9. Two-photon photoemission spectra for clean and bilayer-C_6F_6-covered Cu(111) taken with one-color laser light at $h\nu = 4.15$ eV. See the text for annotations.[51]
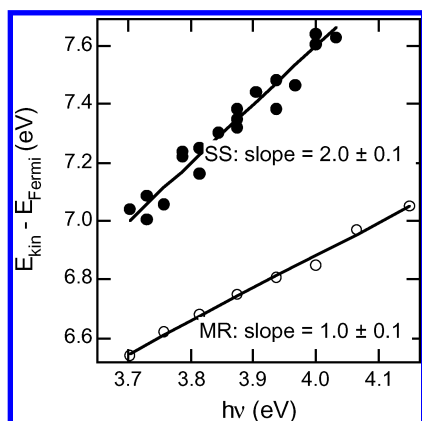

Figure 10. Positions of the MR and SS peaks in Figure 9 as a function of photon energy. The solid lines are linear fits with the indicated slopes.[51]

4. Issues on Interfacial Electron Transport

4.1. Energetic Alignment at Molecule−Metal Interfaces.
The very first question on electron transport at molecule−metal interfaces is where molecular orbitals are located energetically with respect to the metal Fermi level. Although occupied MOs can be characterized by conventional one-photon photoemission spectroscopy, 2PPE is capable of mapping out unoccupied MOs in addition to occupied MOs. The occupied and unoccupied nature of these states is easily distinguished by the dependence of electron kinetic energy on photon energy.

Figure 9 shows as an example 2PPE spectra (one color laser excitation) from a clean and a bilayer-C_6F_6-covered Cu(111) surface.[49−51] The spectrum from the clean Cu(111) surface shows features from the occupied d band, the broad and unoccupied sp band, the occupied surface state (SS), and the unoccupied $n = 1$ image potential state (IS). The adsorption of the C_6F_6 bilayer shows, in addition to features from the Cu-(111) substrate, an adsorbate-induced peak (labeled MR for molecular resonance). The position of the MR peak scales with $1\Delta h\nu$, as shown by open circles in Figure 10, which unambiguously establishes the unoccupied nature. For comparison, the SS peak from the occupied surface state (solid circles) scales with $2\Delta h\nu$. The MR peak is assigned to the σ^* LUMO of C_6F_6 located 3 eV above the metal Fermi level.[49] Compared to the vertical electron affinities of C_6F_6 in the gas and condensed phases (Figure 11), the LUMO level seen here in the adsorbate state is lowered by 1.7 and 0.7 eV, respectively. This lowering can be attributed to the stabilization of the transient anion by
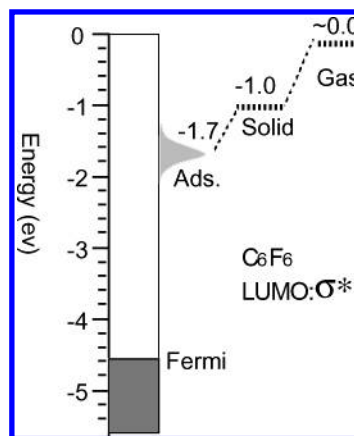

Figure 11. Energetic positions of the σ^* LUMO of C_6F_6 on Cu(111) as compared to the vertical electron affinities of C_6F_6 in the gas and condensed phases.[49]

electronic polarization in surrounding molecules and in the metal substrate; the latter is the image potential.

The lowering of a molecular anionic resonance by the image potential on a metal surface clearly shows the importance of this potential in governing electron transport across a metal−molecule interface. For a nanometer-scale junction, as illustrated in Figure 1A, a tunneling electron should experience image potentials on both electrodes. A recent measurement of a single-electron transistor showed that the apparent HOMO−LUMO gap for a single conjugated molecule is lowered from 2.5 eV in the gas phase to ~0.2 eV when the molecule is contacted by two metal electrodes.[52] Electronic structural calculation attributed this dramatic change to image potential stabilization by the two metal electrodes.

Because intramolecular excitation is not possible over the whole photon energy range investigated, the LUMO must be populated by excitation from occupied metal states (i.e., photoinduced electron transfer in Figure 5A. This excitation mechanism is verified by measurements using polarized light.[53] The direct photoexcitation mechanism in Figure 5A requires strong electronic coupling between the LUMO and the metal substrate. This is puzzling because C_6F_6 is weakly adsorbed on the Cu(111) surface;[49] the Cu surface state is not completely quenched by adsorption (Figure 9). One possible explanation for the strong electronic coupling is that it results from the mixing of the LUMO with image potential states. Image potential states are known to couple strongly to the metal substrate because of the leaky barrier on the metal surface.[36−38] Mixing with the adsorbate layer allows the LUMO to "borrow" electronic coupling strength from image potential states. In fact, an electron in the LUMO is also subjected to the image potential, which is superimposed on the molecular potential. Thus, the measured molecular state should have substantial characteristics of image potential states. Supporting this argument, we note that the LUMO state in the C_6F_6 layer shows significant parallel dispersion, with an effective electron mass only slightly higher than that of the free-electron mass.[50,51] Similar arguments have been made for image potential states at Ar/Cu(100) interfaces.[41]

There are a few other examples where unoccupied states in adsorbate−metal systems have been observed. Wolf and co-workers observed the $2\pi^*$ unoccupied state (located 3.6 eV above the Fermi level) in CO adsorbed on Cu(111).[46,54] It is transiently populated via photoexcitation from occupied metal states. This state possesses π symmetry because the transition dipole moment is found to be oriented in the surface plane, as shown by measurements using s-polarized light. There is strong

Feature Article

J. Phys. Chem. B, Vol. 108, No. 26, 2004 **8787**

electronic coupling between the $2\pi*$ CO state and the Cu substrate, leading to an ultrashort lifetime of only 0.8−5 fs. Angle-resolved measurements showed little parallel dispersion. In another example of alkaline metal atoms adsorbed on transition-metal single-crystal surfaces, the $\sigma*$ antibonding states resulting from chemisorption have been observed in 2PPE.[48] The $\sigma*$ states, populated via direct photoexcitation from occupied bulk metal or surface states, show transient lifetimes ranging from a few femtoseconds to ∼50 fs, depending on the crystalline face of the substrate. The relatively long lifetimes on the (111) faces of Cu and Ag are attributed to the fact that the $\sigma*$ state is located within a gap of the projected bulk band. As a result, resonant charge transfer between the transiently populated $\sigma*$ state and substrate metal bands is inhibited. Such a relatively long lifetime makes it feasible to directly probe electronic−nuclear coupling dynamics in the time domain, as detailed later in section 4.4.

Self-assembled monolayers (SAMs) of thiols on metal surfaces have been popular choices in the field of molecular electronics. The author and co-workers carried out 2PPE studies of thiol SAMs on Cu(111) in conjunction with ab initio calculations.[55] This work revealed the presence of two $\sigma*$ states located 3.2 and 6.4 eV above the Fermi level. These states are spatially localized to the C−S−Cu linker and are assigned to the S−Cu and C−S antibonding orbitals. For symmetry reasons, these localized $\sigma*$ states introduced by the anchoring bond cannot couple to the delocalized $\pi*$ states within a conjugated molecular framework. However, ab initio calculations showed that the π HOMO is delocalized between the molecular framework and the metal surface via the −S− bridge. Harris and co-workers carried out angle-resolved 2PPE measurement on methanethiolate on Ag(111).[56] They observed the $\sigma*$ LUMO 1.6 eV above the Fermi level as well as the HOMO 1.8 eV below the Fermi level. At saturation adsorbate coverage, the $\sigma*$ LUMO showed parallel dispersion with an effective electron mass of $m_{eff} = 0.5m_e$, but the HOMO showed negative dispersion ($m_{eff} = -2m_e$). The latter can be attributed to the π symmetry of the HOMO, which mainly consists of the lone pair of nonbonding p electrons on the S atom. The observed dispersions are evidently substrate-mediated.

2PPE probes the alignment of excitons to the metal Fermi level when the initial excitation is intra- or intermolecular (i.e., mechanism C in Figure 5). This is the case for epitaxial films of C_{60} grown on the Cu(111) surface.[57,58] Figure 12 shows a set of two-photon photoemission spectra from various coverages of C_{60} on Cu(111). Compared to the clean Cu(111) surface, the adsorption of 1 ML of C_{60} completely quenches the surface state, but the image potential states remain. With the exception of image potential states, the spectrum from the C_{60} monolayer is limited to a few weak features superimposed on the copper substrate spectrum. Further increasing the coverage to ≥2 ML leads to a dramatic change in the 2PPE spectrum. Three intense peaks appear to dominate at all coverages investigated. These features remain nearly unchanged when the C_{60} coverage is increased from 2 to 40 ML, which presumably approaches the characteristics of bulk C_{60}. They are assigned to transitions involving the occupied HOMO and unoccupied LUMO + 1 and LUMO + 2 levels, as detailed below. The initial optical excitation is within the molecular film rather than metal-to-molecule interfacial charge transfer, as evidenced by the small change in the 2PPE spectra when the C_{60} coverage is increased from 2 to 40 ML. The photoemission signal originating from an initial metal-to-molecule charge-transfer excitation should diminish with increasing film thickness.
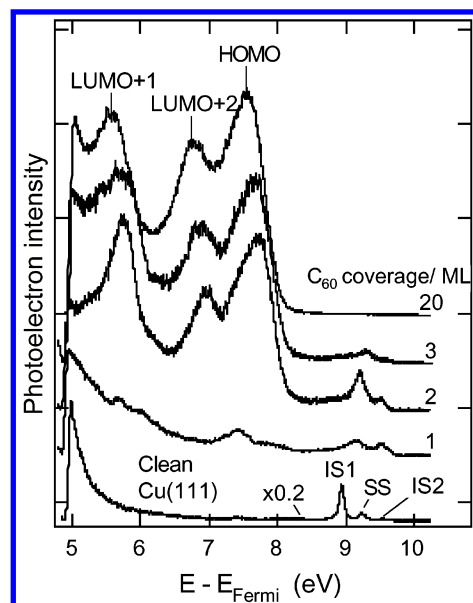

Figure 12. 2PPE spectra taken at a photon energy of 4.83 eV for clean and C_{60}-covered Cu(111) surfaces at various coverages (1−20 ML). The clean Cu(111) spectrum above 8.3 eV is scaled by a factor of 0.2. IS1 and IS2: image potential states ($n = 1$ and 2); SS: surface state.[57,58]
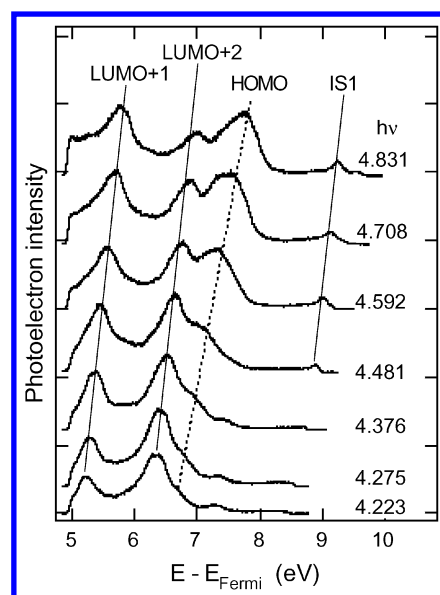

Figure 13. 2PPE spectra of 2-ML C_{60}/Cu(111) taken at the indicated photon energies. The dashed line corresponds to the two-photon dependence of peak position, and the solid lines indicate one-photon dependences. IS1 is the $n = 1$ image potential state.[57,58]

The occupied and unoccupied origins of these transitions are verified by their dependence on photon energy. Figure 13 shows a set of 2PPE spectra taken with the indicated photon energies for two monolayers (ML) of C_{60} on Cu(111). The vertical offset on each spectrum in Figure 13 is chosen to be proportional to the photon energy. Four major peaks are observed in the photon energy range explored. The position (E_{kin}) of one peak scales with $2\Delta h\nu$ (observed at all coverages) and is identified as the highest occupied molecular orbital (HOMO). The positions of other peaks scale with $1\Delta h\nu$. The unoccupied state near the vacuum level is the $n = 1$ image potential state and will be discussed later. The other two unoccupied states are 0.95 and 2.16 eV above E_F; they were previously assigned by Dutton and Zhu as the LUMO and LUMO + 1 in charge-transfer excitons[57] but have recently been reassigned to the LUMO + 1

and LUMO + 2 levels in Frenkel excitons,[58] in agreement with the work of Eberhardt and co-workers.[59,60] The HOMO → LUMO Frenkel exciton is not observed because of the low photon energy used. Note that the relative locations of the HOMO peak, as compared to those of the LUMO + x ($x = 1$, 2) peaks, in a 2PPE spectrum might seem strange at first glance. This ordering results from the fact that the peak labeled HOMO results from coherent two-photon ionization from the HOMO and that those labeled LUMO + x come from first promoting an electron from an occupied level into the unoccupied level followed by photoionization from the transiently populated level. If the initial occupied level is HOMO − y ($y = 1$, 2...), then one expects the kinetic energy of the photoelectron from the LUMO + x level to be lower than that from the HOMO.

4.2. Localized Nature of the Interfacial Electrostatic Potential. Interface formation between molecules and a metal substrate often involves charge redistribution, which can affect the energetic alignment of molecular orbitals to the metal Fermi level and introduce interfacial barriers for charge transport.[5] Charge redistribution at metal/molecule interfaces is fundamentally different than the well-known picture of band bending and Schottky barrier formation at metal/inorganic semiconductor interfaces. In the latter case,[61] interfacial charge redistribution is viewed as spatially delocalized. In the surface normal direction, the electrostatic field extends tens or hundreds of nanometers (depending on doping level) into the semiconductor, forming the so-called space−charge region. In the direction parallel to the surface, the field is often viewed as uniform. Such a picture neglects the atomistic details of bonding at the metal−semiconductor interface. This approximation is justified on the basis of the delocalized nature of electronic states in both metal and semiconductor phases, although challenges to this traditional view have been raised recently.[62]

At metal−molecular solid interfaces, the localized nature of bonding (chemisorption) and the lack of a significant dispersion of electronic states in the molecular solid suggest that one should take a localized view of interfacial charge redistribution. Such a localized view of the electrostatic potential at metal−molecule interfaces has been demonstrated for image potential states in the C_{60}/Cu(111) system.[63] The model system is selected because C_{60} grows epitaxially on Cu(111) to form a 4 × 4 superlattice. There is charge transfer of 1.5−2 electrons per molecule from Cu to the first C_{60} layer. The great extent of charge transfer on Cu(111) and the large molecular diameter (10 Å) of C_{60} are two critical elements contributing to the formation of a large dipole moment for each adsorbed molecule forming the (4 × 4) dipole lattice. Such a dipole lattice provides lateral confinement of the image potential states, which are normally delocalized in the surface plane on clean Cu(111).

As shown in Figure 12, the $n = 1$ and 2 image potential states are present on C_{60}/Cu(111) for C_{60} coverages ≤3 ML. The $n = 1$ image potential state moves toward the vacuum level as the C_{60} coverage increases (binding energy = 0.81, 0.57, and 0.44 eV for 0-, 1-, and 2-ML C_{60}, respectively). Angle-resolved 2PPE measurements are used to establish the dispersion of the $n = 1$ image potential state. The angle of electron detection (θ) is varied in a plane containing the (111) and (11$\bar{2}$) crystal directions. These dispersions are summarized in Figure 14, which shows binding energies of the $n = 1$ image potential state as a functional of the parallel momentum vector. On 1-ML C_{60}/Cu(111), the $n = 1$ image potential state shows no dispersion (bandwidth <0.04 eV). The situation is different on 2-ML C_{60}/Cu(111); here the $n = 1$ peak disperses strongly, with a bandwidth of 0.17 eV. The variation of the parallel momentum
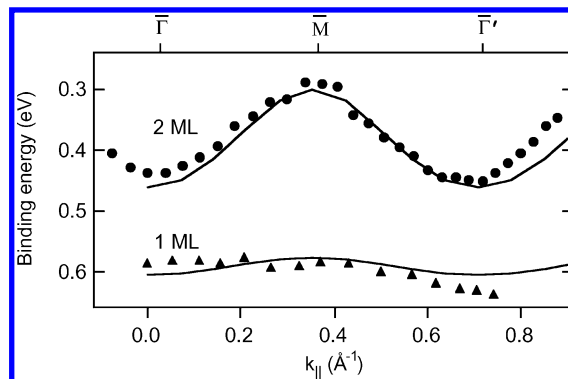

Figure 14. Parallel dispersions of the $n = 1$ image potential state on Cu(111) covered by 1- (▲) and 2-ML (●) C_{60}. $k_{||}$ is the parallel momentum vector. Filled symbols are experimental results; solid curves are from quantum mechanical simulation.[63]

covers multiple Brillouin zones because of the large lattice constant of the C_{60} film. This enables the direct observation of the periodic variation of the $n = 1$ image potential state band structure with $k_{||}$. The presence of the (4 × 4) superlattice is manifested in the umklapp process corresponding to zone folding. Fitting the data near $k_{||} = 0$ to eq 17 gives an effective electron mass of $m_{eff} = 3m_e$.

The lack of dispersion for 1 ML indicates that the image-state wave function is spatially localized. This cannot be attributed to the intrinsic corrugation of the C_{60} monolayer because the same corrugation is also present on the 2-ML covered surface, but the image potential state is delocalized in that case. The observed localization of the $n = 1$ image potential state for the single-monolayer case is attributed to the highly corrugated electrostatic potential generated by the dipole lattice at the interface. Adding a second layer of C_{60} substantially restores the free-electron behavior because of the increased distance of the image electron to the interface and the screening of the dipole potential by the second layer of neutral C_{60} molecules. This interpretation is supported by quantum mechanical simulation using a dielectric continuum model (DCM),[38] with the addition of the periodic electrostatic potential from the dipole lattice.

Each anionic adsorbate within the first layer is treated as a point charge ($q = -2e$) at the center of the molecule. The combination of these point charges with their images in the metal forms the dipole lattice. A 2D model containing the (11$\bar{2}$) crystal direction and the surface normal is used in simulation. The electrostatic potential seen by an electron at vertical distance z (from the metal surface) and lateral coordinate y is given by the sum of the image potential, V_i,[38] and the potential due to the dipole lattice, V_d:

$$V = V_i(z) + V_d(y, z) \qquad (18)$$

where V_d is the 1D lattice sum of the electrostatic potential of the point charges, along with an infinite series of images formed by the dielectric−metal and vacuum−dielectric interfaces. To account further for the geometric corrugation of the C_{60} molecules, a periodic cosine function in the y direction is added to the image potential. Note that this geometric correction is identical for both 1- and 2-ML coverages but could not lead to different observed dispersions. Rather, it accounts for the deviation from free-electron behavior at 2-ML coverage where the effect of the lattice potential is negligible. A 2D Schrödinger equation for the periodic potential is solved numerically to give the simulated dispersions (solid curves in Figure 14) that agree satisfactorily with experimental data.[63]
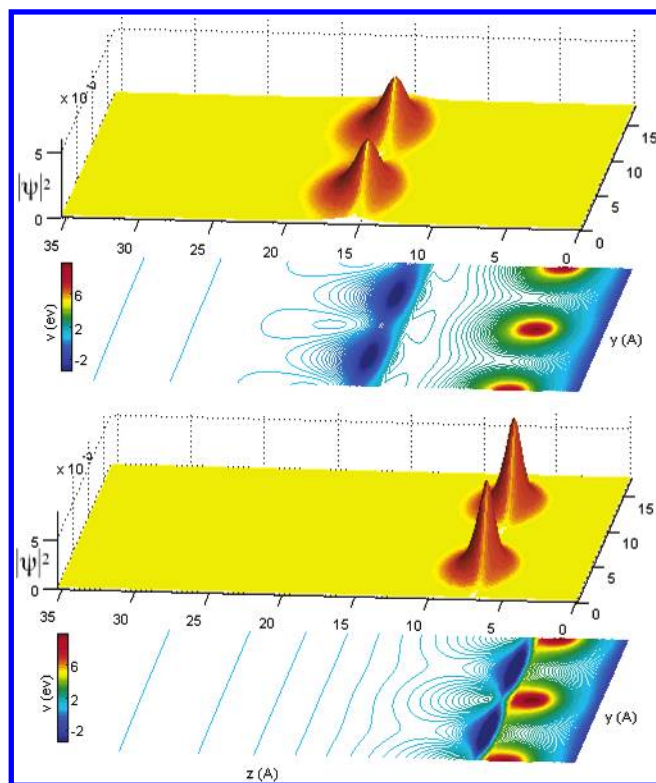
Feature Article

J. Phys. Chem. B, Vol. 108, No. 26, 2004 **8789**

Figure 15. Potential field (*V*) and resulting electron density ($|\Psi|^2$) for the *n* = 1 image potential state on Cu(111) covered by 1- (lower) and 2-ML C_{60} (upper); *z* is the distance from the metal surface, and *y* is lateral distance along the (11$\bar{2}$) crystal direction of Cu. (Dutton, Pu, Truhlar, and Zhu, unpublished results).

Figure 16. (a) Time-resolved 2PPE cross-correlation curves of the molecular resonance on C_6F_6/Cu(111) at the indicated coverages, recorded with $h\nu_1$ = 4.26 eV pump and $h\nu_2$ = 2.13 eV probe pulses. The dotted line indicates zero delay time determined from the cross-correlation signal of the occupied surface state (SS) on clean Cu(111). (b) Lifetimes (population decay) for the molecular resonance as a function of coverage.[50]

Figure 15 shows the calculated electron density for the *n* = 1 image potential state, along with the corresponding potentials. At 1-ML coverage, the dipole lattice introduces significant lateral corrugation into the potential in the region where the image electron is predominantly located. This corrugation, along with geometric corrugation, completely confines the wave function within each unit cell. At 2-ML coverage, the effect of the dipole lattice on the image electron is negligible because of the increased distance from the interface. The only corrugation in the electrostatic potential comes from a geometric effect. As a result, the wave function is partially delocalized.

The demonstration of a dipole lattice confirms the necessity of a localized view of electrostatic potentials resulting from interfacial charge redistribution. When the interface is disordered, these individual dipoles may serve as scattering centers. When they are ordered, the periodic potential from the dipole lattice provides a lateral confinement of all delocalized electronic states. The presence of these individual dipoles may affect the coupling between interfacial states and bulk bands, the lateral transport of charge at the interface, and interfacial electron transport.

4.3. Interfacial Electronic Coupling and Spectral Density. As shown in eqs 1 and 2, both the conductance and interfacial electron-transfer rate are proportional to the electronic coupling strength or spectral density. 2PPE is capable of quantifying the spectral density. When an unoccupied molecular orbital is populated via direct photoexcitation from occupied metal states, as is the case for the LUMO of C_6F_6 adsorbed on Cu(111) (Figure 9), the peak width in the 2PPE spectrum is directly related to the spectral density, Γ. However, complications due to inhomogeneous broadening, vibronic broadening, and instrument broadening may make the width determination difficult. A more reliable approach comes from lifetime measurements,
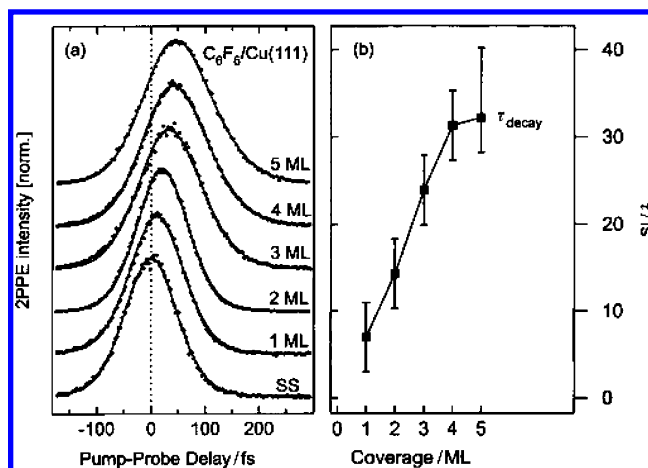
assuming that the decay of the transient state is dominated by electron transfer to the metal substrate. The spectral density is related to the lifetime from the uncertainty principle (eq 9).

Figure 16a shows a set of pump–probe measurements for the σ* LUMO in C_6F_6/Cu(111).[50] Fitting to experimental data yields τ_{decay} shown in panel b. The decay time increases from ~7 fs at 1-ML to ~32 fs at 5-ML coverage. These lifetimes correspond to Γ values of 0.1–0.02 eV for coverages in the range of 1–5 ML. The electronic coupling strength between the LUMO and the metal surface weakens as the film thickness increases. This can be explained by delocalization (dispersion) in the surface normal direction. With increasing film thickness, the center of gravity of the electron density is further away from the metal, thus decreasing its coupling to the metal substrate. Although C_6F_6 is weakly adsorbed on the Cu(111) surface, the lifetime of ~7 fs for the LUMO at monolayer coverage is of the same order of magnitude as those in strong chemisorption systems. For example, the lifetime of the π* anionic resonance in CO chemisorbed on Cu(111) was measured to be 0.8 < τ < 5 fs by time-resolved 2PPE and the spectral line width,[54] and those for the σ* antibonding states in alkali atoms on metal surfaces range from a few femtoseconds to a few tens of femtoseconds.[48] As stated earlier, the strong electronic coupling seen here may result from the mixing of the C_6F_6 LUMO with image potential states (i.e., the molecular state "borrows" electronic coupling strength from image potential states).

Distance-dependent electronic coupling between excited molecules and the metal substrate is also seen for excitons in C_{60}/Cu(111). Figure 17 shows a set of cross-correlation (CC) measurements for the LUMO + 1 level in a Frenkel exciton in C_{60}/Cu(111). In the experiment, the photoelectron signal at the LUMO + 1 peak in the 2PPE spectrum (Figures 12 and 13) is recorded as a function of the pump–probe delay time. The dashed curves are autocorrelation (AC) traces obtained from coherent two-photon ionization of the HOMO. Cross-correlation curves from the LUMO + 1 are broader than the AC function, indicating finite lifetimes for the transiently populated level. If one assumes a single-exponential decay with lifetime of τ_{life}, then the experimental CC data above the constant background can be described by the sum of the AC function (so-called coherent artifact) and an incoherent component that is a convolution of the AC function and a symmetric exponential
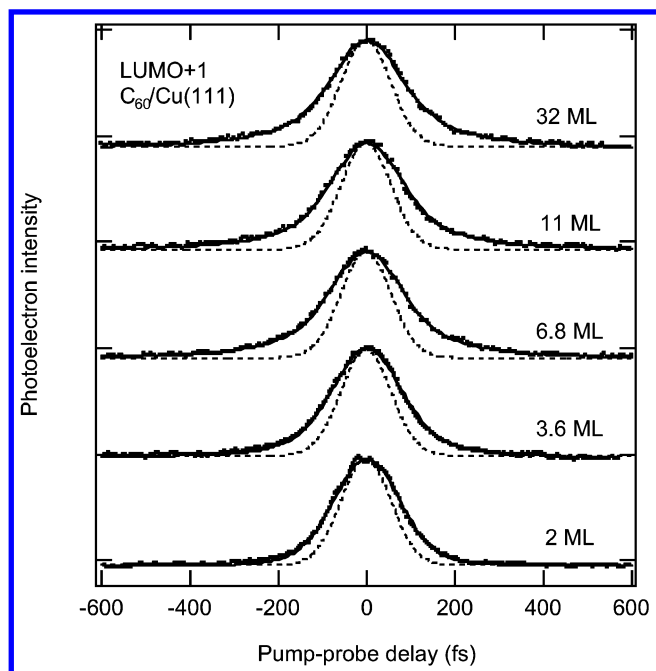
Figure 17. Pump−probe cross correlation (dots) of the LUMO + 1 level in C_{60}/Cu(111) at the indicated coverages (2−32 ML). The solid lines are fits as described in the text. The dashed lines are the autocorrelation curves determined from cross correlation of the HOMO. All curves are normalized with respect to the peak intensities.[58]
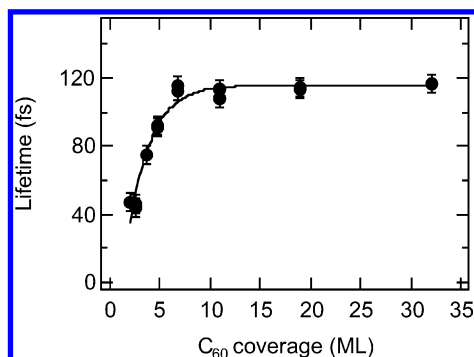

Figure 18. Dependences on film thickness of transient lifetimes for the LUMO + 1 (●). The solid line is an exponential fit.[58]

decay function (equal to zero on both sides of the delay).[64,65] This fitting (solid curves in Figure 17) gives the lifetime at each C_{60} coverage, as summarized in Figure 18. The solid line in Figure 18 is the fit of the coverage-dependent lifetime to a simple exponential function, with an asymptotic value of $\tau_a = 116 \pm 5$ fs.

As shown in Figure 18 for C_{60} coverages >6 ML, the decay dynamics is independent of film thickness and must be attributed to intrinsic mechanisms in solid C_{60}. The exact mechanism of such an ultrafast decay is not known, but one can identify two likely candidates. Following the initial photoexcitation of an electronic exciton, electron−nuclear interaction can lead to the formation of polaron excitons, also called self-trapped excitons. The formation of self-trapped excitons can occur on an ultrafast time scale (i.e., the inverse of the vibrational frequency involved). Such a self-trapping process does not lead to a significant decrease in the energetic position of the electron in the LUMO + 1 but may result in a substantial change (decrease) in the transition dipole moment for photoionization. In addition, an exciton involving the LUMO + 1 level may decay rapidly into a lower-lying exciton involving the LUMO. Note that a
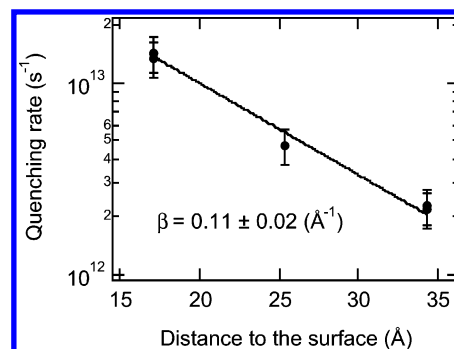

Figure 19. Dependences of substrate quenching rates for the LUMO + 1 (●) as a function of distance to the Cu(111) surface. The solid is fit to eq 5, which yields the indicated β value.[58]

self-trapped exciton may decay on a much slower time scale, but this kind of slow dynamics is not followed here.

The LUMO + 1 lifetime decreases exponentially with decreasing film thickness because of quenching by Cu. An efficient quenching channel is charge transfer between the excited molecule and the metal substrate. Such a charge-transfer mechanism is well established in the extensive literature of photochemistry on metal surfaces.[7,8,25] Efficient electron transfer between donor molecules and photoexcited C_{60} is also well known in solution-phase studies.[66] Quenching of an electronic exciton in the C_{60} film by the Cu substrate may occur via the transfer of the transient electron in the LUMO + 1 level to unoccupied metal bands above the Fermi level. One can semiquantitatively establish the distance dependence in quenching rates. At an intermediate coverage (≤6 ML), the decay rate ($1/\tau$) from each state can be approximated by the sum of two relaxation channels: the intrinsic decay rate, $1/\tau_a$, where τ_a is 116 fs, and an external quenching rate, k_q, due to charge transfer to the Cu substrate. The substrate quenching rates obtained from this analysis are shown as a function of distance to the metal surface in Figure 19. The distance dependence in electron-transfer rates (k_{ET}) is often described by an exponential function of the form of eq 5, where the β parameter ($Å^{-1}$) characterizes the nature of the bridge in mediating electron transfer within a tunneling picture. Fitting the data in Figure 19 gives a β value of 0.11 ± 0.02 $Å^{-1}$, which is significantly smaller than typical values for tunneling through molecular bridges.[14] The fitting also gives the projected rate constant at zero distance, k_0, which is 9.0×10^{13} s^{-1}. This rate constant corresponds to electronic coupling strength of $\Gamma = 0.06$ eV as estimated from eq 9.

Within the picture of strong electronic coupling, it is inadequate to describe charge transfer between an exciton in C_{60} and the Cu substrate as tunneling. Instead, one should view this process as direct electronic coupling mediated by delocalized electronic bands. Theoretical studies predict a bandwidth of 400−600 meV for LUMO/HOMO bands in solid C_{60}.[67] Within this strong-coupling picture, the coverage dependence in the quenching rate can be understood as follows: with increasing C_{60} thickness, $|\Psi|^2$ within a delocalized C_{60} band is, on average, further away from the Cu surface; as a result, its overlap with the Cu substrate decreases. At coverages >6 ML, the charge-transfer quenching mechanism cannot compete with the intrinsic lifetimes within solid C_{60}.

The two examples shown above are relevant to interfacial electron transport in molecule-based conventional devices. Future experiments using time-resolved 2PPE on systems of interest to single-molecule devices, such as self-assembled monolayers on metal surfaces, are clearly warranted. How does interfacial electronic coupling (Γ) depend on the nature of the

Feature Article

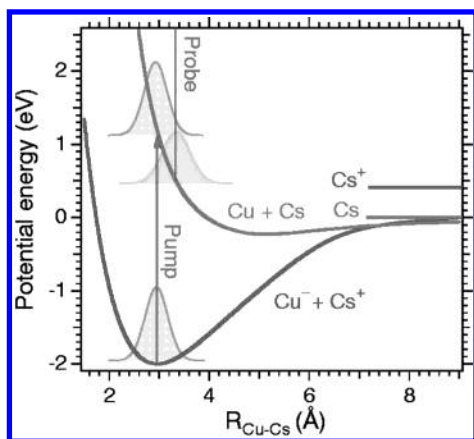*J. Phys. Chem. B, Vol. 108, No. 26, 2004* **8791**

Figure 20. Schematic potential energy surfaces for the photodesorption of Cs from the Cu(111) surface. The pump pulse projects the ground-state wave packet onto the excited state, "turning on" the repulsive forces. The evolving wave packet is detected by the delayed probe pulse-induced photoemission from the σ^* ($6s + 6p_z$) antibonding state.[68]

chemical bond (i.e., anchor) to the surface? This is probably the most important and interesting question.

4.4. Electronic−Nuclear Coupling and Dynamic Localization. The strong tendency of electronic−nuclear coupling and charge-carrier localization is a salient feature of molecule-based electronics. In molecular semiconductors for conventional devices, polaron formation and hopping is the dominant mechanism for carrier transport.[33] In single-molecule-based devices, such as a metal−molecule−metal tunneling junction, electronic−nuclear coupling cannot be ignored when electron tunneling occurs at or near a resonance because the tunneling traversal time increases substantially.[2] In fact, this kind of coupling may play a key role in interesting transport phenomena such as negative differential resistance or switching. Recent 2PPE experiments have demonstrated the feasibility of directly probing the dynamics of electronic−nuclear coupling.

Petek and co-workers applied the experimental scheme illustrated in Figures 6 to follow the dynamics of electronic−nuclear coupling in the model system of Cs atoms chemisorbed on Cu(111).[48,68] The experiment is illustrated using model potential energy surfaces in Figure 20. The first photon initiates electron transfer from the metal (the occupied surface state) to the σ^* resonance (antibonding or repulsive state in terms of chemisorption). The ensuing nuclear dynamics on the repulsive potential energy surface is reflected in a decrease in the final-state electron energy due to relaxation in the intermediate σ^* state, as illustrated by the nuclear wave packet dynamics within a Born−Oppenheimer picture on the model potential energy surfaces. The experimental data from 2PPE measurement is shown in Figure 21A, where the peak position of the σ^* resonance is plotted as a function of the pump−probe delay time; the σ^* state relaxes as much as 0.25 eV at a time delay of 160 fs. The decrease in electronic energy can be converted to a change in the nuclear coordinate (i.e., the Cu−Cs bond distance, Figure 21B) based on the repulsive potential energy surface in Figure 20.

Harris and co-workers applied time- and angle-resolved 2PPE to follow the localization dynamics of an initially delocalized electron wave function in the molecular phase.[69] This is achieved in the model system of image potential states on ultrathin alkane layers on Ag(111). In the experiment, the pump photon excites an electron from an occupied metal state to the unoccupied image ($n = 1$) state, and after certain time delay, the probe photon ionizes the image potential state for detection. As
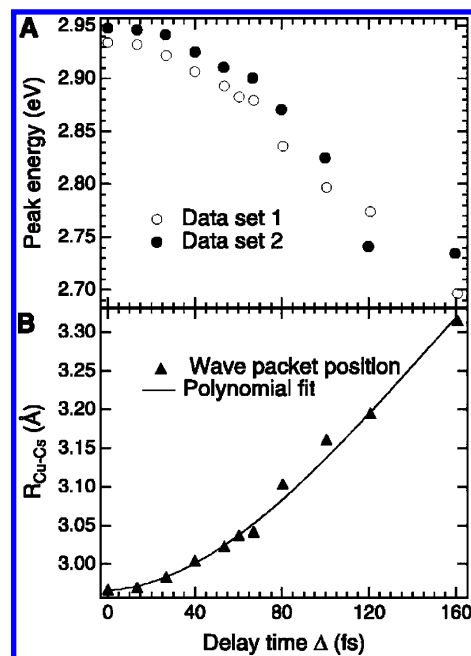

Figure 21. (A) Peak position above E_{Fermi} in 2PPE spectra of the σ^* LUMO as a function of the pump−probe delay time for ∼0.09-ML Cs/Cu(111). (B) Wave packet position $R_{Cu−Cs}$ obtained from the data in panel A and the potential energy surface in Figure 20.[68]
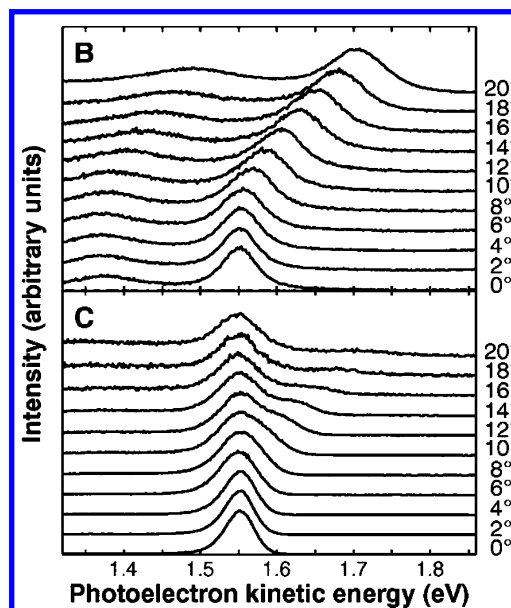

Figure 22. Femtosecond angle-resolved 2PPE spectra in the $n = 1$ image potential state region for bilayer *n*-heptane−Ag(111) taken at pump−probe delay times of 0 (B) and 1670 fs (C). Initially, the electron is in the delocalized state with $m^* = 1.2m_e$. The electron then becomes localized within a few hundred femtoseconds (after Ge et al.).[69]

expected, the nascent image electrons are delocalized in the direction parallel to the surface plane. This is demonstrated by angle-resolved 2PPE spectra in Figure 22. The dispersion at zero time delay shows nearly free-electron behavior, with an effective electron mass of $1.2m_e$. With increasing delay time (Δ_t), the extent of dispersion diminishes and completely disappears for $\Delta_t > 1$ ps. These initially delocalized electrons self-trap to form 2D small polarons within the alkane adlayer. The authors also successfully modeled the energy and temperature dependences of localization within the activated polaron formation model (similar to that shown in Figure 2 and described

by eq 14). Similar approaches were recently used to study electron solvation dynamics at molecule−metal interfaces.[70,71]

The two examples demonstrated above clearly show that time-resolved 2PPE is capable of directly establishing the role of electronic−nuclear coupling in systems of interest to molecule-based electronics. For interfacial charge transport in molecular electronics, a time-dependent 2PPE experiment (e.g., relaxation in energy) essentially allows us to see "switching" or dissipation during electron transport in the time domain. For conventional electronics based on organic semiconductors, a time- and angle-resolved 2PPE experiment will allow us to establish the energetics and rates of polaron formation directly from an initially free conduction-band electron. This information is necessary in quantitatively establishing the possibility of a bandlike transport mechanism at low temperatures and its transition to a polaron hopping mechanism at high temperatures. These experiments on molecule-based electronics are currently being investigated by us and others.

Comments

In the last a few years, we have witnessed a tremendous surge in excitement and activity in the field of molecule-based electronics, particularly in so-called molecular electronics where a single molecule or a small group of molecules serve as active electronic components. Such excitement is warranted, considering the attractiveness of molecules as electronic components in terms of size and structural control, self-assembly and chemical recognition, dynamical stereochemistry, and synthetic tailorability.[1] However, this kind of excitement is also a reason for caution. As in most newly emerging or reemerging fields, there have been a large number of phenomenological demonstrations in the field of molecular electronics, but fundamental studies based on well-controlled model systems are lacking. In this regard, theoretical descriptions of tunneling at molecular junctions are more advanced than experimental probes; one can easily arrive at this conclusion by counting the number of theoretical and experimental papers in a recent issue of *Chemical Physics* dedicated to "transport in molecular wires".[72] Testing or challenging these theories cannot come from device transport measurements alone. Rather, one should resort, in a major way, to the time-proven approaches of experimental physical chemistry (i.e., spectroscopy). Experiments on two-photon photo-emission spectroscopy exemplify a small step forward in this undertaking. The success of this spectroscopic view is demonstrated by the direct connection between quantities probed in 2PPE experiments and key components in theories. In many ways, the molecular electronics problem is a surface problem. Surface spectroscopists should bear the responsibility for establishing an experimental foundation toward a quantitative understanding in molecular electronics.

References and Notes

(1) Heath, J. R.; Ratner, M. A. *Phys. Today* **2003**, *56*, 43.
(2) Nitzan, A. *Annu. Rev. Phys. Chem.* **2001**, *52*, 681.
(3) Nitzan, A.; Ratner, M. A. *Science.* **2003**, *300*, 1384.
(4) Ishii, H.; Sugiyama, K.; Ito, E.; Seki, K. *Adv. Mater.* **1999**, *11*, 605.
(5) Cahen, D.; Kahn, A. *Adv. Mater.* **2003**, *15*, 271.
(6) Miller, R. J. D.; McLendon, G. L.; Nozik, A. J.; Schmickler, W.; Willig, F. *Surface Electron-Transfer Processes*; VCH: New York, 1995.

(7) Zhu, X.-Y. *Annu. Rev. Phys. Chem.* **1994**, *45*, 113.
(8) Zimmermann, F. M.; Ho, W. *Surf. Sci. Rep.* **1995**, *22*, 127.
(9) Hagfeld, A.; Gratzel, M. *Chem. Rev.* **1995**, *95*, 49−68.
(10) Asbury, J. B.; Hao, E.; Wang, Y.; Shosh, H. N.; Lian, T. *J. Phys. Chem. B* **2001**, *105*, 4545.
(11) Gosavi, S.; Marcus, R. A. *J. Phys. Chem. B* **2000**, *104*, 2067.
(12) Tully, J. *J. Chem. Phys.* **1998**, *109*, 7702.
(13) Brandbyge, M.; Hedegaard, P.; Heinz, T. F.; Misewich, J. A.; Newns, D. M. *Phys. Rev. B* **1995**, *52*, 6042.
(14) Adams, D. M.; Brus, L.; Chidsey, C. E. D.; Creager, S.; Creutz, C.; Kagan, C. R.; Kamat, T. V.; Lieberman, M.; Lindsay, S.; Marcus, R. A.; Metzger, R. M.; Michel-Beyerle, M. E.; Miller, J. R.; Newton, M. D.; Rolison, D. R.; Sankey, O.; Schanze, K. S.; Yardley, J.; Zhu, X. *J. Phys. Chem. B* **2003**, *107*, 6668.
(15) Wold, D. J.; Haag, R.; Rampi, M. A.; Frisbie C. D. *J. Phys. Chem. B* **2002**, *106,* 2813.
(16) Schmickler, W. *J. Electroanal. Chem.* **1986**, *204*, 31.
(17) Boroda, Y. G.; Voth, G. A. *J. Chem. Phys.* **1995**, *104*, 6168.
(18) (a) Holstein, T. *Ann. Phys.* **1959**, *8*, 325. (b) Holstein, T. *Ann. Phys.* **1959**, *8*, 343.
(19) Emin, D. *Phys. Today* **1982**, *June*, 34.
(20) Keller, C.; Stichler, M.; Comelli, G.; Esch, F.; Lizzit, S.; Menzel, D.; Wurth, W. *Phys. Rev. B* **1998**, *57*, 11951.
(21) Keller, C.; Stichler, M.; Comelli, G.; Esch, F.; Lizzit, S.; Wurth, W.; Menzel, D. *Phys. Rev. Lett.* **1998**, 80, 1774.
(22) Keller, C.; Stichler, M.; Fink, A.; Feulner, P.; Menzel, D.; Foehlisch, A.; Hennies, F.; Wurth, W. *Appl. Phys. A* **2004**, *78*, 125.
(23) Landauer, R. *Phys. Rev. Lett.* **1981**, *85*, 91.
(24) Newns, D. M. *Phys. Rev.* **1969**, *178*, 1123.
(25) Gadzuk, J. W. *Phys. Rev. B* **1991**, *44*, 13466.
(26) Wingreem, N. S.; Jacobsen, K. W.; Wilkins, J. W. *Phys. Rev. B* **1989**, *40*, 11834.
(27) Ho, W. *J. Chem. Phys.* **2002**, *117*, 11033.
(28) Park, J. et al. *Nature* **2002**, *417*, 722.
(29) Segal, D.; Nitzan, A.; Ratner, M.; Davis, W. B. *J. Phys. Chem. B* **2000**, *104*, 2790.
(30) Segal, D.; Nitzan, A.; Davis, W. B.; Wasielewski, M. R.; Ratner, M. *J. Phys. Chem. B* **2000**, *104*, 3817.
(31) Gadzuk, J. D. *Annu. Rev. Phys. Chem.* **1988**, *39*, 395.
(32) Seideman, T. *J. Phys.: Condens. Mater.* **2003**, *15*, R521.
(33) Silinsh, E. A.; Capek, V. *Organic Molecular Crystals: Interaction, Localization, and Transport Phenomena*; AIP Press: Woodbury, NY, 1994.
(34) Echenique, P. M.; Pendry, J. B. *J. Phys. C* **1978**, *11*, 2065.
(35) Echenique, P. M.; Pendry, J. B. *Prog. Surf. Sci.* **1990**, *32*, 111.
(36) Fauster, T.; Reuss, C.; Shumay, I. L.; Weinelt, M. *Chem. Phys.* **2000**, *251*, 111.
(37) Fauster, Th.; Steinmann, W. In *Photonic Probes of Surfaces*; Halevi, P.; Ed.; Elsevier: Amsterdam, 1995.
(38) Harris, C. B.; Ge, N.-H.; Lingle, R. L., Jr.; McNeil, J. D.; Wong, C. M. *Annu. Rev. Phys. Chem.* **1997**, *48*, 711−744.
(39) Osgood, R. M., Jr.; Wang, X. *Solid State Phys.* **1998**, *51*, 1−80.
(40) Marinica, D. C. et al. *Phys. Rev. Lett.* **2002**, *89*, 046802.
(41) Berthold, W.; Rebentrost, F.; Feulner, P.; Höfer, U. *Appl. Phys. A* **2004**, *78*, 131.
(42) Ge, N. H.; Wong, C. M.; Harris, C. B. *Acc. Chem. Res.* **2000**, *33*, 111.
(43) Gaffney, K. J.; Miller, A. D.; Liu, S. H.; Harris, C. B. *J. Phys. Chem. B* **2001***, 105*, 9031.
(44) Zhu, X.-Y. *Annu. Rev. Phys. Chem.* **2002**, *53*, 221.
(45) Petek, H.; Ogawa, S. *Prog. Surf. Sci.* **1998**, 56, 239.
(46) Wolf, M.; Hotzel, A.; Knoesel, E.; Velic, D. *Phys. Rev. B* **1999**, *59*, 5926.
(47) Velic, D.; Knoesel, E.; Wolf, M. *Surf. Sci.* **1999**, *424*, 1.
(48) Petek, H.; Nagano, H.; Weida, M. J.; Ogawa, S. *J. Phys. Chem. B* **2001**, *105*, 6767.
(49) Vondrak, T.; Zhu, X.-Y. *J. Phys. Chem. B* **1999**, *103*, 3449.
(50) Gahl, C.; Ishioka, K.; Zhong, Q.; Hotzel, A.; Wolf, M. *Faraday Discuss.* **2000**, *117*, 191.
(51) Dutton, G.; Zhu, X.-Y. *J. Phys. Chem. B* **2001**, *105*, 10912
(52) Kubatkin, S. Danilov, A.; Hjort, M.; Cornil, J.; Bredas, J.-L.; Stuhr-Hasen, N.; Hedegard, P.; Bjornholm, T. *Nature* **2003**, *425*, 698.
(53) Gahl, C. Diploma Thesis, Fritz-Haber-Institute, Berlin, 1999.
(54) Bartels, L.; Meyer, G.; Rieder, K.-H.; Velic, D.; Knoesel, E.; Hotzel, A.; Wolf, M.; Ertl, G. *Phys. Rev. Lett.* **1998**, *80*, 2004.
(55) Vondrak, T.; Wang, H.; Winget, P.; Cramer, C. J.; Zhu, X.-Y. *J. Am. Chem. Soc.* **2000**, *122*, 4700.
(56) Miller, A. D.; Gaffney, K. J.; Liu, S. H.; Szymanski, P.; Garret-Roe, S.; Wong, C. M.; Harris, C. B. *J. Phys. Chem. A* **2002***, 106*, 7636.
(57) Dutton, G.; Zhu, X.-Y. *J. Phys. Chem. B* **2002**, *106*, 5975.
(58) Dutton, G.; Zhu, X.-Y. *J. Phys. Chem. B,* submitted for publication, 2004.
(59) Jacquemin, R.; Kraus, S.; Eberhardt, W. *Solid State Commun.* **1998**, *105*, 449

(60) Link, S.; Scholl, A.; Jacquemin, R.; Eberhardt, W. *Solid State Commun.* **2000**, *113*, 689.

(61) Ludeke, R. In *Handbook of Surface Science*; Horn, K., Scheffler, M.; Eds.; Elsevier: Amsterdam, 2000; Vol. 2.

(62) Tung, R. T. *Phys. Rev. Lett.* **2000**, *84,* 6078.

(63) Dutton, G.; Pu, J.; Truhlar, D. G.; Zhu, X.-Y. *J. Chem. Phys.* **2003**, *118*, 4337.

(64) Ogawa, S.; Petek, H. *Surf. Sci.* **1996**, *357−358*, 585.

(65) Knoesel, E.; Hotzel, A.; Wolf, M. *Phys. Rev. B* **1998**, *57*, 12812.

(66) Guldi, D. M.; Kamat, P. V. In *Optical and Electronic Properties of Fullerenes and Fullerene-Based Materials*; Shinar, J., Vardeny, Z. V., Kafafi, Z. H., Eds.; Marcel Dekker: New York, 2000; p 225.

(67) Dresselhaus, M. S.; Dresselhaus, G.; Eklund, P. C. *Science of Fullerenes and Carbon Nanotubes*; Academic Press: New York, 1996.

(68) Petek, H.; Nagano, H.; Weida, M. J.; Oagawa, S. *Science* **2000**, *288*, 1402.

(69) Ge, N.-H.; Wong, C. M.; Lingle, R. J., Jr.; McNeill, J. D.; Harris, C. B. *Science* **1998**, *279*, 202.

(70) Miller, A. D.; Bezel, I.; Gaffney, K. J.; Garrett-Roe, S.; Liu, S. H.; Szymanski, P.; Harris, C. B. *Science* **2002**, *297*, 1163.

(71) Gahl, C.; Bovensiepen, U.; Frischkorn, C.; Wolf, M. *Phys. Rev. Lett.* **2002**, *89*, 107401.

(72) Hänggi, P.; Ratner, M.; Yaliraki, S., Eds. *Chem. Phys.* **2002**, *281*, 111−502 and all publications therein.